The Astrophysical Journal, 967:37 (13pp), 2024 May 20 https://doi.org/10.3847/1538-4357/ad3b90

Age Determination of LAMOST Red Giant Branch Stars Based on the Gradient Boosting Decision Tree Method

Hai-Feng Wang[1], Giovanni Carraro[1], Xin Li[2], Qi-Da Li[3], Lorenzo Spina[4], Li Chen[5], Guan-Yu Wang[2], and Li-Cai Deng[6]
[1] Dipartimento di Fisica e Astronomia "Galileo Galilei," Università degli Studi di Padova, Vicolo Osservatorio 3, I-35122, Padova, Italy; haifeng.wang.astro@gmail.com, giovanni.carraro@unipd.it
[2] Department of Astronomy, China West Normal University, Nanchong, 637002, People's Republic of China
[3] Yunnan Observatories, Chinese Academy of Sciences, Kunming 650216, People's Republic of China
[4] INAF-Padova Observatory, Vicolo dell'Osservatorio 5, 35122 Padova, Italy
[5] Shanghai Astronomical Observatory, Chinese Academy of Sciences, 80 Nandan Road, Shanghai 200030, People's Republic of China
[6] National Astronomical Observatories, Chinese Academy of Sciences, Beijing 100101, People's Republic of China
Received 2023 October 28; revised 2024 March 22; accepted 2024 April 5; published 2024 May 16

Abstract

In this study, we estimate the stellar ages of LAMOST DR8 red giant branch (RGB) stars based on the gradient boosting decision tree (GBDT) algorithm. We used 2643 RGB stars extracted from the APOKASC-2 asteroseismological catalog as the training data set. After selecting the parameters ([α/Fe], [C/Fe], $T_{\rm eff}$, [N/Fe], [C/H], log g) highly correlated with age using GBDT, we apply the same GBDT method to the new catalog of more than 590,000 stars classified as RGB stars. The test data set shows that the median relative error is around 11.6% for the method. We also compare the predicted ages of RGB stars with other studies (e.g., based on APOGEE) and find some systematic differences. The final uncertainty is about 15%–30% compared to the ages of open clusters. Then, we present the spatial distribution of the RGB sample with an age determination, which could recreate the expected result, and discuss systematic biases. All these diagnostics show that one can apply the GBDT method to other stellar samples to estimate atmospheric parameters and age.

Unified Astronomy Thesaurus concepts: Milky Way disk (1050); Stellar ages (1581); Red giant branch (1368); Catalogs (205)

1. Introduction

The Milky Way (MW) is a unique laboratory for Galactic archeological studies because a large number of individual stars can be precisely resolved. Multidimensional information can be used to study the properties of stellar populations and the history of our Galaxy. The abundance of chemical elements on the surface of stars can be used to provide fossil evidence of the Galactic environment at the time of their birth. In turn, stellar ages are helpful in tracing the history of the MW. Therefore, it is essential to estimate reliable stellar ages for widely distributed stars across the MW (Martig et al. 2016a; Gallart et al. 2019; Conroy et al. 2022; Xiang & Rix 2022; Anders et al. 2023; Ciucă et al. 2024).

Red giant branch (RGB) stars are evolved stars in which H is burning in a shell surrounding a growing core of helium. On the other hand, red clump giant (RCG) stars typically form a distinct horizontal branch on the H-R diagram, which can be mixed with the RGB. These stars are burning helium in their core. In terms of stellar populations, RGB stars are particularly beneficial for Galactic archeology (e.g., Stello et al. 2015; Anders et al. 2023). They are numerous and cover a wide range of stellar ages (Miglio et al. 2012). Because of their high luminosity, RGB stars can be observed at larger distances, thus probing all the way to the outskirts of our Galaxy. Moreover, their solar-like oscillations may be observed at longer frequencies than those required to observe similar oscillations in dwarf and subgiant stars (Schonhut-Stasik et al. 2024).

Accurate stellar age estimation for large samples is essential for a comprehensive understanding of the structure, kinematics, and dynamics of different stellar populations in the MW (Wang et al. 2018a, 2018b, 2019, 2020a, 2020b, 2020c, 2022a, 2023a, 2023b; López-Corredoira et al. 2018; Silva Aguirre et al. 2018; Mackereth et al. 2019; Ness et al. 2019; Chen et al. 2021; Lu et al. 2022; Li et al. 2023). However, it is difficult to estimate stellar ages directly from the observations, and one has to rely on empirical formulae (e.g., Soderblom 2010). To circumvent all this, the abundance ratio [α/Fe] is often used as an age proxy (Rix & Bovy 2013; Bovy et al. 2016; Kordopatis et al. 2023).

Stellar evolution models have often been employed to estimate stellar ages by comparing stellar parameters inferred from observations with model predictions. A practical approach to age estimation of individual field stars is to use spectroscopic and/or photometric methods (Fitzpatrick 1999; Brott & Hauschildt 2005; Bouret et al. 2008; Gustafsson et al. 2008; Shulyak et al. 2017; Andrae et al. 2023; Zhang et al. 2023), to derive stellar photospheric parameters and compare the inferred star positions in the Hertzsprung–Russell (H-R) diagram with theoretical tracks and/or isochrones (Santiago et al. 2016; Mints & Hekker 2017; McMillan et al. 2018; Sanders & Das 2018; Lebreton & Reese 2020). However, it is not easy to apply this method to RGB giants because the isochrones of giant stars of different ages suffer from severe mixing effects on the H-R diagram and are not precise enough (Soderblom 2010; Noels & Bragaglia 2015). Another effective method (but also dependent on models) is provided by asteroseismology (Chaplin & Miglio 2013), which can be used to estimate the age of field stars, including red giants. However, it has not been applied yet to large enough samples.

With the advent of surveys, such as APOGEE (Majewski et al. 2017), many measurements of stellar parameters have become available that can be used to estimate ages. The stellar surface properties $\log g$ and $T_{\rm eff}$ can be used to characterize stellar spectroscopic type and luminosity class. Then, in combination with theoretical stellar evolution models, one may obtain information on stellar ages (Bressan et al. 2012; Choi et al. 2016; Scilla 2016). However, stellar evolution induces changes in the surface chemical abundances through physical processes such as *dredge-up*, where CNO products (nitrogen-rich and carbon-poor) are brought up into the stellar atmosphere. These CNO processes depend on mass, and therefore abundance ratios, such as the carbon-to-nitrogen ratio [C/N], can provide deep insights into stellar evolution and can be used to estimate age (Salaris et al. 2015). Thus, information about stellar evolution (i.e., age) is also correlated with [Fe/H], [α/Fe], and other chemical abundances (Nissen 2015, 2016; Tucci Maia et al. 2016; Feltzing et al. 2017; Nissen et al. 2017; Spina et al. 2018; Casali et al. 2019; Jofré et al. 2020; Casamiquela et al. 2021; Viscasillas Vázquez et al. 2022). Finally, the measured stellar abundances depend on the material from which the star formed (Spina et al. 2016; Delgado Mena et al. 2019; Ness et al. 2019).

Ness et al. (2016) and Martig et al. (2016b) determined stellar masses from spectroscopy, which greatly extends the range of giant stars with age estimates. They showed that the masses and implied age (Masseron & Gilmore 2015; Lagarde et al. 2017; Huang et al. 2020) of post-dredge-up giants can be measured from high-resolution infrared spectra (APOGEE (Wilson et al. 2019), $R \approx 22{,}500$), and the correlation of masses and ages with $T_{\rm eff}$, $\log g$, [M/H], [C/M], and [N/M]. This study has increased the number of giant stars of known age to 70,000.

Ness et al. (2015) described a data-driven stellar modeling method called Cannon that allows for spectral mass measurements, and Ho et al. (2017a) used Cannon to transfer labels from a high-resolution, high signal-to-noise ratio (S/N) survey (APOGEE) to a low-resolution, medium-S/N survey (LAMOST). The author showed that using Cannon, the fundamental parameters ($T_{\rm eff}$, $\log g$, [Fe/H], and [α/M]) consistent with the APOGEE values can be determined directly from the LAMOST spectra. They applied the model to 450,000 giants from LAMOST DR2 that were not observed by APOGEE, and this dramatically increased the number and sky coverage of stars with mass and age estimates. Ting et al. (2018) also estimated 175,202 red clump (RC) stars in LAMOST with 3% contamination and also included two asteroseismology parameters, ΔP and $\Delta\nu$.

However, until the arrival of the PLATO mission (Rauer et al. 2014; Miglio et al. 2017), red giants ages from the common constraints of asteroseismology and spectroscopy have only been applicable to specific samples in certain fields, such as Kepler (e.g., Pinsonneault et al. 2014, 2018; Wu et al. 2018; Miglio et al. 2021), CoRoT (Valentini et al. 2016; Anders et al. 2017), K2 (e.g., Rendle et al. 2019; Zinn et al. 2022), or TESS continuum observing regions (Sharma et al. 2018; Silva Aguirre et al. 2020; Mackereth et al. 2021; Wu et al. 2023). Thus, large-scale spectroscopic surveys, such as APOGEE (Majewski et al. 2017), GALAH (De Silva et al. 2015), and LAMOST (Cui et al. 2012) have been dedicated to providing empirical spectroscopic-based age estimates for Galactic archeological studies, and asteroseismic data are simply used as benchmarks (e.g., Martig et al. 2016b; Leung & Bovy 2019; He et al. 2022). Such large samples of stellar spectroscopic ages provide great scientific value for Galactic studies, even if their accuracy is below the ideal requirement (Xiang et al. 2019; derived from Payne; see Ting et al. 2019). In this work, we use the stellar ages analyzed by Pinsonneault et al. (2018) based on APOGEE spectral parameters and Kepler asteroseismic data as the training sample.

Asteroseismology is considered to be one of the most accurate ways to obtain stellar ages so far. Currently, spectral ages obtained from the asteroseismology data set have a number of limitations. Leung et al. (2023) proposed addressing these issues by applying a variational encoder-decoder on cross-domain astronomical data. The model was trained on stellar pairs from both APOGEE and Kepler observations, and these APOGEE spectra could then be trained to predict ages with about 1000 precise asteroseismic stellar ages. The model produces more accurate spectral ages for APOGEE DR17 ($\sim$22% overall and $\sim$11% for RC stars) compared to previous data-driven spectral ages. However, due to the lack of asteroseismic parameters, we have chosen to use machine-learning algorithms in our work to determine stellar ages using correlations between stellar feature parameters and ages.

As for machine learning, one can rely on a training set with high-quality stellar parameters and then apply the tool to predict a large sample of stellar ages. So far, many astronomical data measurements have been based on machine-learning algorithms (Ting & Rix 2019; Ting et al. 2019; Ciucă et al. 2021; Hayden et al. 2022). Using the third data release of the GALAH survey, Buder et al. (2021) recently demonstrated that by using supervised machine-learning regression, specifically the popular extreme gradient boosting (XGBoost) method (Chen & Guestrin 2016), it is possible to infer the *spectrum* (or chemistry) of main-sequence turn-off stellar ages with an accuracy of 1–2 Gyr. He et al. (2022) performed a similar exercise using the same technique but employing RC stars observed by the LAMOST survey (which has the advantage of providing C and N abundances), trained on Kepler's asteroseismic ages. These authors derived a statistical uncertainty of 31%. Similar accuracy was obtained earlier by Mackereth et al. (2019) using a Bayesian convolution neural network and APOGEE DR14 data trained on APOGEE-Kepler data (Pinsonneault et al. 2018).

Li et al. (2022) used random forest methods and convex-hull algorithms to predict RGB and RCG masses based on scikit-learn (Pedregosa et al. 2011), and hence, RCG ages. The median relative error is 13% for a large sample of K giant masses and 9% and 18% for RC stellar masses and ages, respectively. When compared with the age of the open cluster, the uncertainty is about 10%. For the first time, to the best of our knowledge, they quantitatively compared different machine-learning methods and found that nonlinear models are generally better than linear models. Therefore, the aim of our present study is to develop new algorithms for determining the RGB ages of a large sample of stars, while attempting to improve the accuracy of age predictions as much as possible. In this paper, we use the stellar ages in APOKASC-2 as a training sample and estimate the ages of more than 590,000 stars classified as RGB stars from LAMOST DR8 using the gradient boosting decision tree (GBDT) algorithm.

This paper is structured as follows. In Section 2, we present the data used in this paper. In Section 3, we present the specific

application of the GBDT algorithm to our work. Section 4 shows our age prediction results and compares them with the literature, discussing the advantages and disadvantages of different methods. In Section 5, we discuss the possibility of predicting age with other feature parameters. Section 6 summarizes our conclusions.

2. Data

The results of a machine-learning regressor are very dependent on the quality of the training data set. Therefore, it is better to use a small but statistically significant and high-quality data set during the training stage (Anders et al. 2017). Pinsonneault et al. (2018) provided stellar parameters for 6676 evolved stars in APOKASC-2, which included stellar ages. These ages come from their model using mass, radius, [Fe/H], and [α/Fe]. They adopted a new combination of five methods of asteroseismic measurements to calibrate the inferred stellar parameters. The precision is good enough for us to predict ages and has already been widely used in the community. In this paper, we use stars marked as RGB in APOKASC-2 to train the age prediction model.

We selected 3777 stars marked as RGBs in APOKASC-2 and crossmatched them with LAMOST DR8 to get a sample of 2643 stars. We excluded some stars with large errors using the GBDT prediction first, so only high-precision sources were retained. Finally, we obtained 2087 stars of which 1047 were used for the training and 1040 for testing during the machine-learning process.

In Figure 1, the top panel shows a Kiel plot of our RGB samples for the final high-resolution asteroseismology data set, with the colors indicating the accuracy of the age. The bottom panel contains the RGB targets for age determination from LAMOST DR8, where it is clear that the surface gravity and effective temperature are consistent with K-type RGB stars. As a complement, we also show the age and [C/N] pattern for the same sample (APOKASC-2) in Figure 2, which shows a good correlation up to 10 Gyr. However, the quality of the statistical data deteriorates beyond this age threshold.

Wang et al. (2022b) provided a value-added catalog for LAMOST DR8,[7] which includes 7.1 million stellar parameters estimated from low-resolution spectra. The catalog provides the values of stellar atmospheric parameters (effective temperature $T_{\rm eff}$, surface gravity, log g, metallicity [Fe/H]/[M/H]), the α-element-to-metallicity ratio [α/M], carbon-to-iron abundance ratios [C/Fe] and [N/Fe], and other stellar parameters. In this study, we adopt the chemical abundances of Wang et al. (2022b). Note that there might have been chemical outliers in that work, but this is not the topic of this paper. Our study is based on APOKASC-2 to train the model for age prediction.

Wang et al. (2023c) selected 696,680 RGB stars, 180,436 primary RC stars, and 120,907 secondary RC stars from LAMOST DR8 based on large frequency spacing ($\Delta\nu$) and period spacing (ΔP). The purity and completeness of the RGB and RC samples are both over 95% and 90%, respectively. We used the RGB provided by Wang et al. (2023c), but the age prediction-related parameters needed in this paper are almost all null or spurious in some of the stars. The cleaning of the sample produced 596,116 stars. Kiel diagrams of all the remaining stars are also shown in the lower panel of Figure 1, with the colors indicating the density of the stars in a log scale. We apply the GBDT machine-learning trained age prediction model to this large catalog to provide reliable ages.

[7] In principle, we could use the criteria of $T_{\rm eff}$ and log g in Liu et al. (2014) to select the LAMOST DR10 K giants and choose whether or not to separate them into RGBs and RCGs. Then, we would be able to determine the basic abundance and finally obtain the age. However, this should be addressed in future work. In this work, we only want to explore and test the method for determining the age, so we adopt the publicly available data set and try to improve it .

3. Method

3.1. GBDT

In this paper, we adopt the GBDT algorithm based on the scikit-learn Python package (Pedregosa et al. 2011), which is an additive model based on the idea of boosting integrated learning. It is an iterative decision tree algorithm, also called a multiple additive regression tree. It works by constructing a set of weak learners (trees) and accumulating the results of multiple decision trees as the final prediction output. Weak learners often refer to learners that generalize slightly better than randomly generated results (e.g., classifiers with slightly more than 50% accuracy on binary classification problems). The algorithm effectively combines decision trees with integration ideas.

A decision tree is a basic classification and regression method. The model consists of a tree structure, which can be considered as a collection of the so-called *if-then* rules. At the same time, decision tree algorithms require less feature engineering than other algorithms since they can handle data with missing fields well. Decision trees are able to combine multiple features automatically. And the multiple decision trees are integrated by gradient boosting, which can eventually solve the overfitting problem well. The hyperparameters can be found in the publicly available package.

For GBDT, we set the parameters n_estimators = 100, loss = ls, learning_rate = 0.1, subsample = 1, criterion = friedman_mse, max_depth = 3, min_samples_leaf = 1, min_samples_split = 2, and max_features = None. n_estimators specifies the number of weak classifiers. Increasing this value can improve accuracy, but beyond a certain point, the improvement becomes limited. Loss is used to specify the loss function, where ls stands for least squares regression, learning_rate is used to adjust the contribution of each tree, subsample is used to fit the number of samples for individual learners, criterion measures the regression effects criterion, friedman_mse indicates an improved mean square error, max_depth specifies the maximum depth of individual regression estimates, min_samples_leaf specifies the minimum number of samples required in a leaf node, min_samples_split specifies the minimum number of samples required for a split at each internal node (non-leaf node), max_features limits the number of features to be considered when finding the optimal split.

3.2. Feature Parameter Selection

First, we extracted the importance of the features in the training samples using GBDT, normalized them, and produced the sorting shown in Figure 3. The importance of the features reflects the contribution of that feature in the predicting model, from left to right, [α/Fe], [C/Fe], $T_{\rm eff}$, [N/Fe], [C/H], log g, [M/H], [Fe/H], and [N/H]. However, these degrees of importance are relative, not absolute. All feature parameters also have some correlation with each other, as shown in Figure 4. Nonetheless, we make use of Figure 3 to estimate the age in this study. Therefore, it is not necessary to use all the

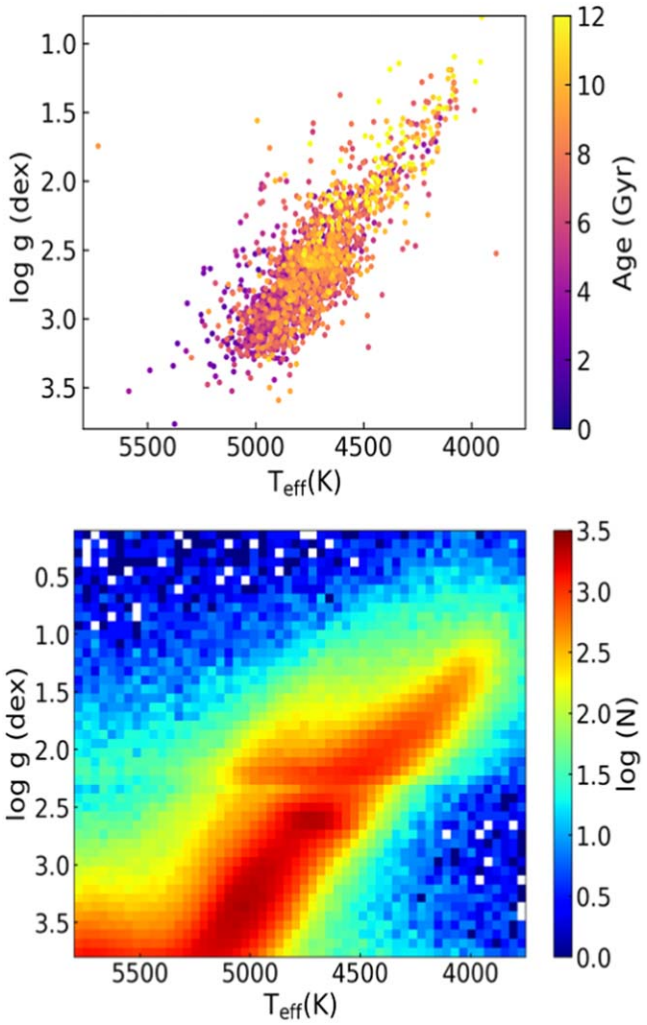

Figure 1. $T_{\rm eff}$–log g diagram of the sample used in this paper. The upper panel shows a Kiel diagram of the RGB stars selected from the APOKASC-2 catalog as the final small training sample, and the colors indicate the stellar ages. The lower panel shows a Kiel diagram of the large sample to be estimated using the GBDT method. The sample of RGB is identified by Wang et al. (2023c) from LAMOST DR8, with purity and completeness exceeding 95%.

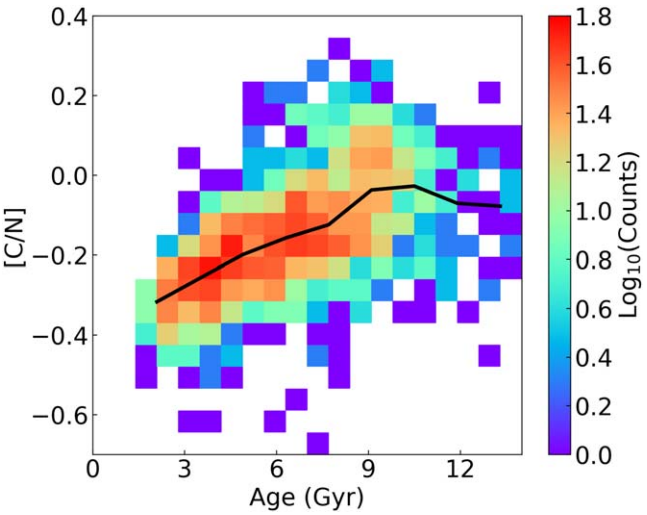

Figure 2. [C/N]–age diagram of the training sample used in this paper, with the color indicating the stellar density in the log scale showing that both parameters are correlated with each other.

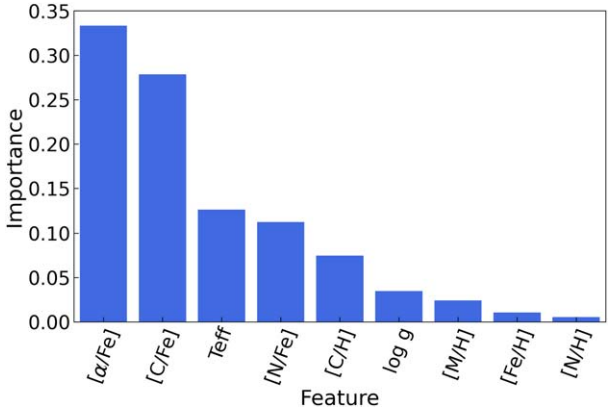

Figure 3. Stellar feature parameters extracted using the GBDT algorithm. The stellar features are sorted from left to right in order of importance, with the importance reflecting the contribution of that feature in the prediction model.

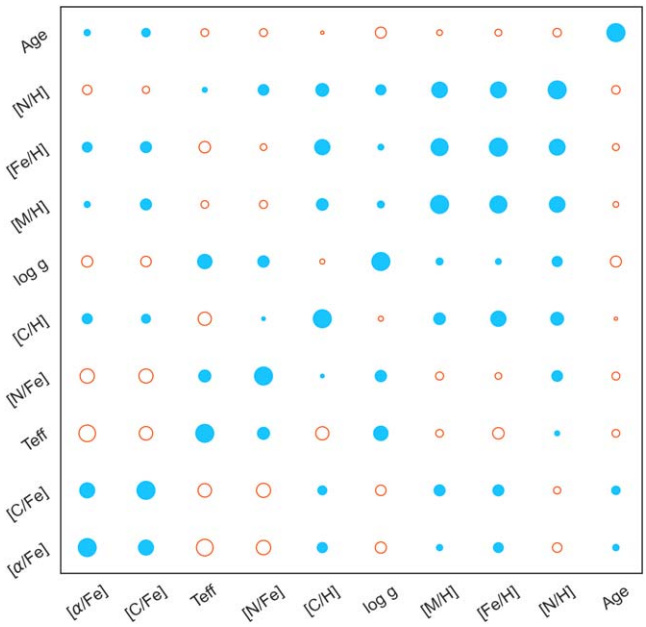

Figure 4. Confusion matrix for all parameters, with red indicating a positive correlation and blue indicating a negative correlation. Note that this is for the training sample, and we reasonably chose to condition the importance analysis to estimate age as shown in Figure 3.

feature parameters for model training, but rather select the first few highly correlated ones from them as a reasonable input.

It is found that there is a high correlation between all these stellar features by testing (discussed in the Appendix), so it is feasible to select the top few features in the order of importance to predict the age. Therefore, we increase the number of features in the model for the age prediction and calculate the average relative error each time. The average relative error at different numbers of features is shown in Figure 5. It can be seen that the average relative error decreases as the number of stellar features increases. Therefore, we finally select the first six features ([α/Fe], [C/Fe], $T_{\rm eff}$, [N/Fe], [C/H], log g) for the training of the predicted age model.

3.3. Performance on the Test Data Set

The results of our model on the test data set are shown in Figure 6. The upper panel shows the predicted age compared to the APOKASC-2 test sample age and the dispersion, and the

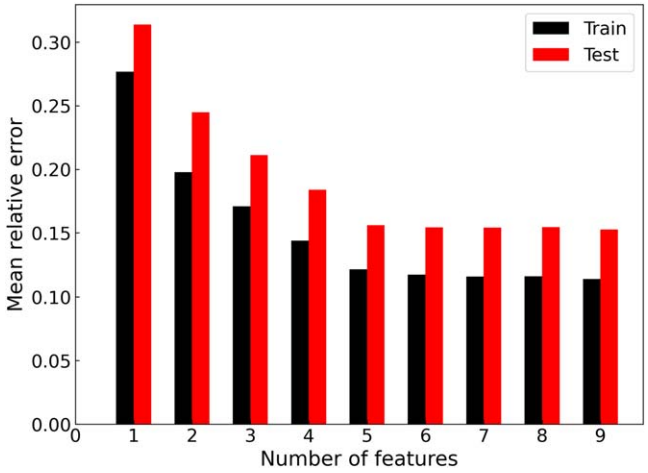

Figure 5. The average relative error between the training and test data sets as the number of training stellar features varies. The black histograms indicate the training data set, and the red histograms indicate the test data set. The figure indicates the average relative error of the most stable value when there are six features.

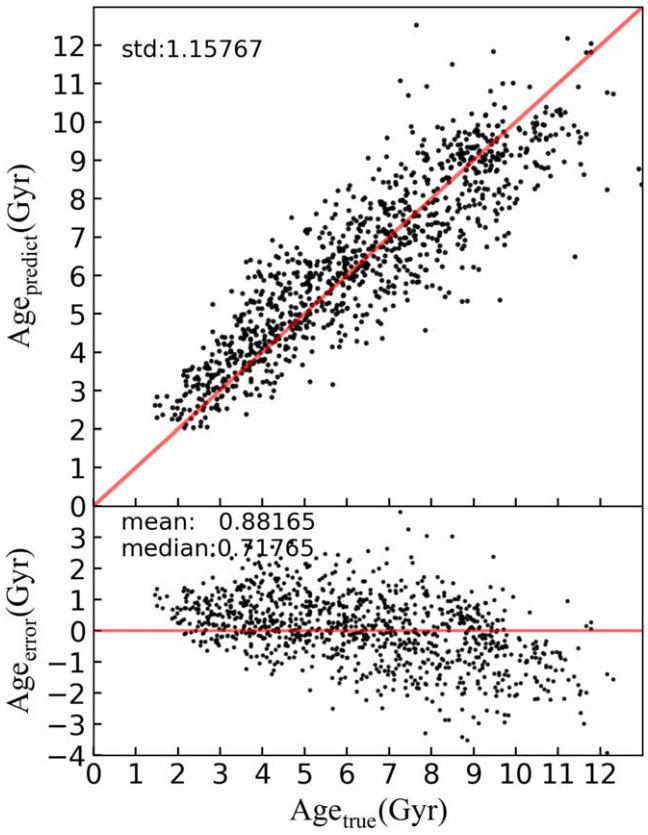

Figure 6. Error analysis of the predicted ages for the test sample. The black dots denote the ages in the test sample, the *x*-axis represents the true value, the *y*-axis represents the predicted value, and the solid red lines are there to guide the eye to see the performance of the method. The dispersion is calculated by subtracting the predicted age from the literature in the test set and then taking the standard deviation. The absolute error is the predicted value minus the true value.

lower panel shows the absolute age error versus the true age and the mean and median of the absolute errors. We see that in the comparison of the predicted age to the original age, the scatter points and the red line exhibit a similar trend, indicating that the predicted age coincides with the true age. The points

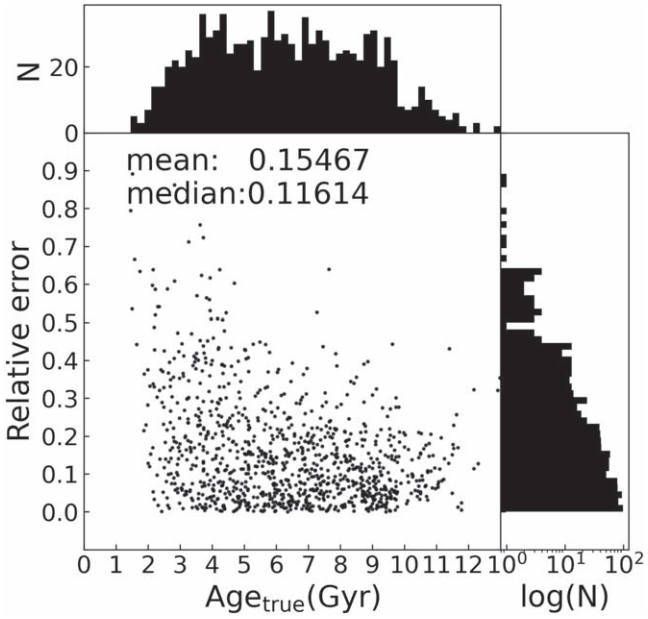

Figure 7. The mean and median relative error of predicted age for the test data set. The black dots represent the relative error in age, the top histogram is the star counts, and the right panel shows the distribution of the relative age error in terms of values. The relative error is the absolute error divided by the true values. It is naturally found that the errors should be small since they are from the same catalog but divided into testing and training.

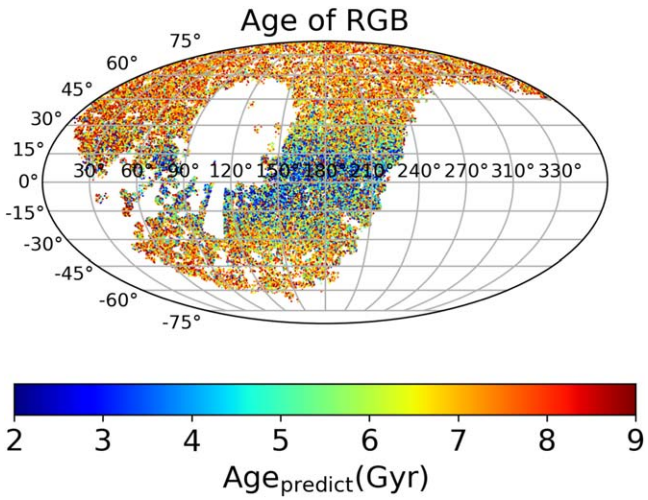

Figure 8. Distribution of the predicted RGB stars ages in Galactic coordinates.

that do not fall on the solid red line are also evenly distributed on both sides of the line, and the dispersion of the predicted age is 1.16 Gyr. The absolute error has a similar distribution, with a mean and median of 0.88 and 0.72 Gyr, respectively. Note that in order to ensure that the range of parameter distributions in both the training data set and the test data set are uniformly covered with respect to the range of the total sample distribution, we adopt the following data partitioning method: we randomly extract the star from the training and test data set, trying to keep both data sets almost equal.

In addition, in Figure 7, we show the mean[8] and median relative errors of the ages predicted by the model for the test

[8] As the standard mathematical definition, the residuals between the predicted value and the *true value* of the original data set are calculated, and then the residuals are divided by the true value.

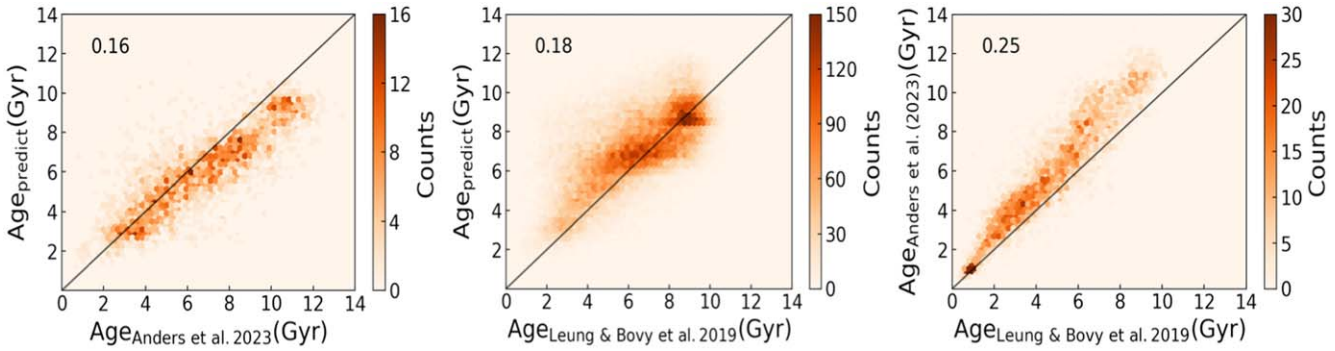

Figure 9. Comparison of the ages predicted in this paper with the results of Anders et al. (2023; left panel), Leung & Bovy (2019; middle panel), and the results of Anders et al. (2023) compared with those of Leung & Bovy (2019; right panel). Colors indicate the number of stars in the bin. The black line is used to guide the eye for the perfect matching. The number in the upper left corner of each subplot is provided by the median relative error.

data set, as well as the distribution of the relative age errors with age. The relative error is the absolute error derived above divided by the true value. The average relative error of our predicted stellar ages is 15%, with a median relative error of 12%. Because machine learning will autonomously search for relevant patterns from the training sample, if we can have a much larger number of training samples with higher accuracy, then our prediction accuracy can be improved further.

The top histogram of Figure 7 shows that the ages of our training sample are almost homogeneously distributed, with a smaller number of older stars. We also note that in the lower panel of Figure 6, the prediction errors for older stars are often below the red line, implying that our age predictions for older stars may be weak, in line with that found in other studies. Possible reasons are that the training data set may have a limited number of samples for older stars, or the features of these samples may not be accurately or comprehensively represented, causing the model to fail to accurately learn and understand the features of older stars, resulting in underestimated age predictions. Insufficient feature selection is also a factor. The performance of the GBDT model heavily relies on the selection and representation of features. If the selected features fail to capture the key characteristics of older stars, or the feature representation is not comprehensive enough, the model may struggle to accurately predict the age of older stars.

In the future, we plan to use a new machine-learning method to extract pure RGB stars and exploit a larger suite of chemical abundances based on LAMOST DR10/DR11. This way, we might be able to estimate ages more accurately.

4. Results

In this section, we show the distribution of the final predicted ages in Galactic sky coordinates. We also provide the distribution of the predicted age-relative error analysis carefully and compare it with the literature in order to show that our method and age results are reasonable. Furthermore, we compare our predicted ages with those of open clusters. Although they do not constitute an absolute benchmark, we can still use them to search for a final statistical uncertainty. We also show the correlation between [C/N] and the age of RGB stars, as well as the spatial distribution of the predicted ages.

4.1. Final Stellar Age Distribution

As mentioned, six basic stellar features or the input parameters ([α/Fe], [C/Fe], $T_{\rm eff}$, [N/Fe], [C/H], log g) are used to determine the ages of 596,116 RGB stars in the GBDT framework. Its distribution is shown by the Galactic sky coordinates in Figure 8, with age represented by color. One can readily see that, as expected, at lower latitudes, there are mostly younger stars, while at higher latitudes, the stars tend to be older.

4.2. Further Comparisons of Stellar Age Determinations

In Figure 9, we compare our stellar ages predicted using the GBDT algorithm with the results of other age prediction studies. The age determinations from two previous independent works are based on APOGEE DR17 RGB giants, employing machine-learning methods and similar training samples. Anders et al. (2023) used the XGBoost algorithm, which is applied to the APOGEE-Kepler (Miglio et al. 2021) observations of 3060 RGB and RC stars with high-quality asteroseismic ages. Leung & Bovy (2019) presented the astroNN algorithm, suited to determine not only stellar atmospheric parameters, but also distances and ages from APOGEE spectra. The astroNN age estimation follows the procedure outlined in Mackereth et al. (2019), and the training set is composed of the APOKASC-2 catalog (Pinsonneault et al. 2018) and a sample of 96 low-metallicity stars from Montalbán et al. (2021). This method depends on the relationship between the surface metallicity of RGB stars and their main-sequence mass determined at the time of the star's first dredge-up.

As can be seen in the left two panels of Figure 9, our results are more compatible with Leung & Bovy (2019) than with Anders et al. (2023). The median relative random errors are similar, amounting to $\sim$16%, but the systematics are not the same. In order to highlight the systematics we compare the ages given by Leung & Bovy (2019) with those given by Anders et al. (2023). The results indicate that the systematics of both studies are evident, and the ages from Anders et al. (2023) are systematically larger than the ones from Leung & Bovy (2019), with an average of about 1–2 Gyr.

The age estimate from Anders et al. (2023) is about 1.2 times smaller than the age estimate from astroNN, and our age estimate agrees relatively well with the age estimate from astroNN. Systematic biases are unavoidable and very hard to quantify, especially in the case of RGB stars, and are related to the physics assumptions about mass loss, mixing, rotation, and so forth. There are also sizeable statistical uncertainties (Noels & Bragaglia 2015).

We compare our predicted ages with additional studies, as shown in Figure 10, which together with Figure 9, validates our approach. In the top-left panel to the bottom-right panel of

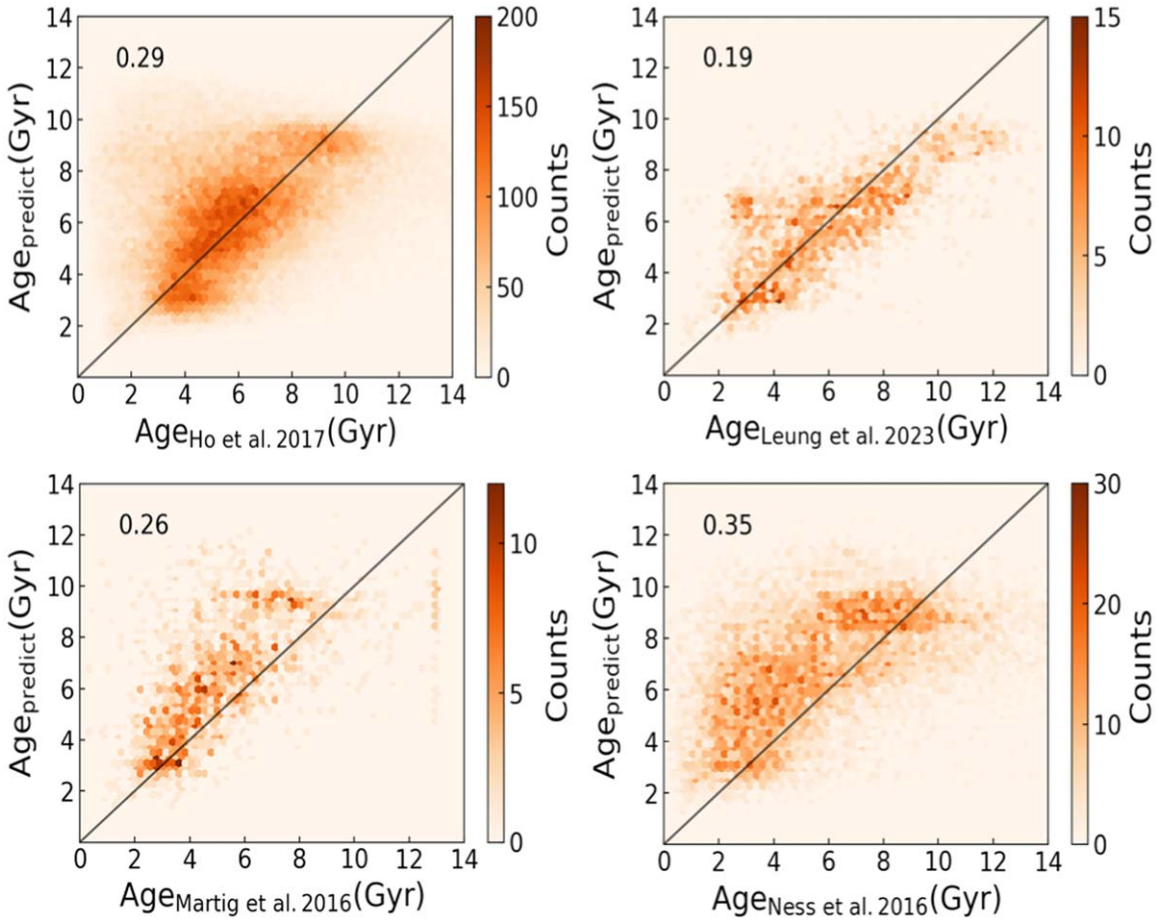

Figure 10. The ages derived from the predictions in this paper are compared with the stellar ages derived in other studies. The results of Martig et al. (2016b), Ho et al. (2017a), Leung et al. (2023), and Ness et al. (2016) are compared with our results from the top-left panel to the bottom-right panel. The relative error is shown in the left-top corner.

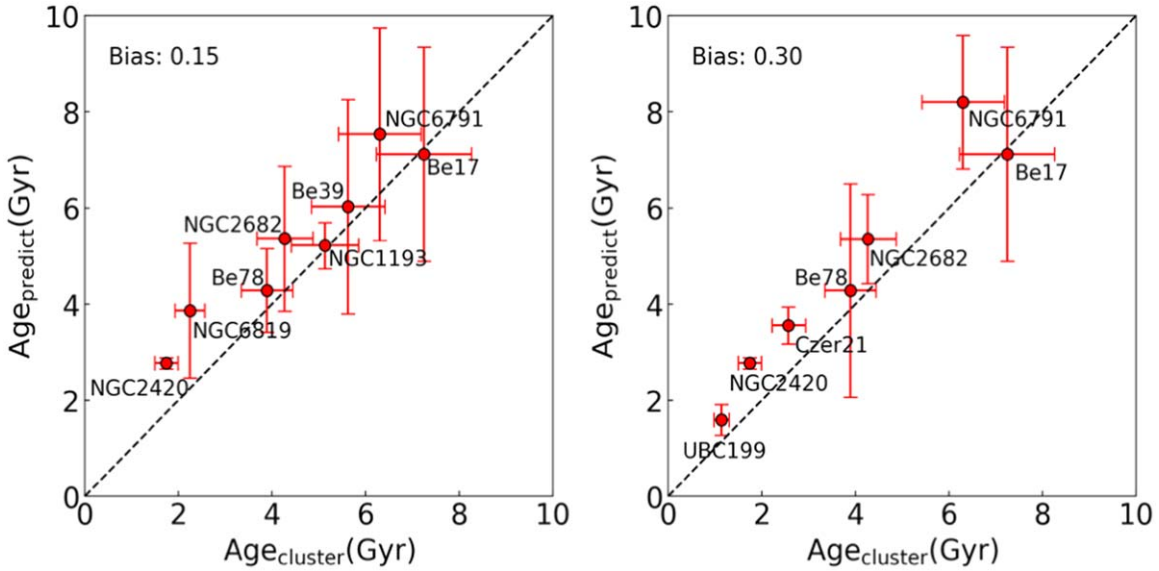

Figure 11. Based on the catalog provided by Cantat-Gaudin et al. (2020), we compare the literature values of open clusters with our predictions. The horizontal error bars represent the uncertainty quoted by Cantat-Gaudin et al. (2020), and the error bars on the *y*-axis denote the standard deviations of the cluster members, which are selected by the distribution of the open cluster. The final bias for the open cluster is shown at the top. The cluster member stars in the left panel are selected using the steps in Figure 12, and the right panel member stars are obtained by directly crossmatching them with the sky coordinate of the cluster member stars provided by Cantat-Gaudin et al. (2020).

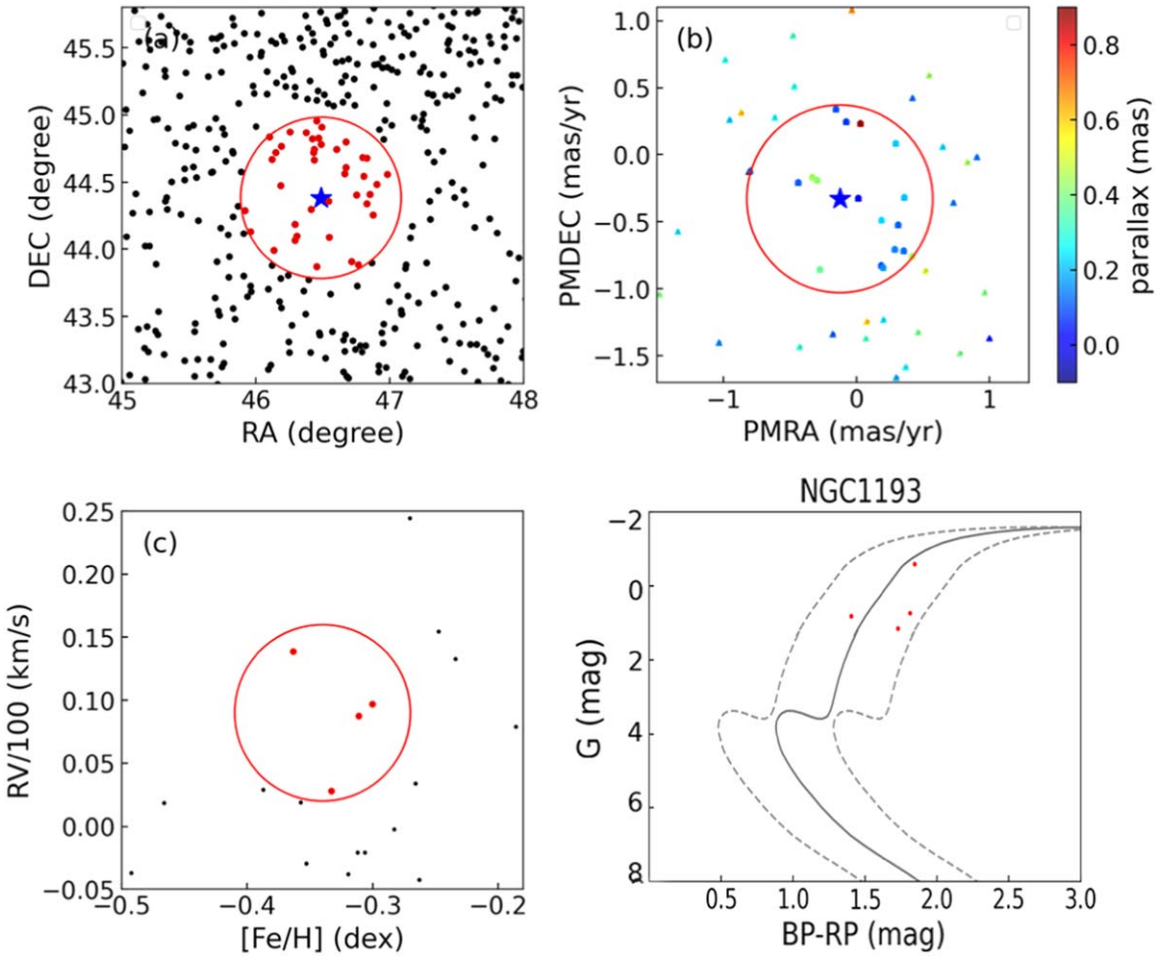

Figure 12. The selection process for membership of open clusters is illustrated using NGC 1193 as an example. The alphabetical order in each panel represents the order in which the cluster members were selected. The blue pentagram denotes the equatorial sky coordinate and proper motion of NGC 1193. The stars in the red circle indicate the members we have selected at this step. The solid gray line represents the isochrone for NGC 1193 with 5.13 Gyr, and the two dashed lines indicate a deviation of 0.4 mag.

Figure 10, we compare our predicted ages with those of Martig et al. (2016b), Ho et al. (2017a), Leung et al. (2023), and Ness et al. (2016), respectively. The figure shows that for stars with an age estimate the comparison is reasonable. The errors range from 19%–35%.

We remind the reader that Ho et al. (2017b) used Cannon to construct predictive models for LAMOST low-resolution spectra. To convert [C/M] and [N/M] to mass and age, they used formulas for the coefficient representations in Tables A2 and A3 of Martig et al. (2016b). These formulas are, in turn, derived from asteroseismic mass measurements of stars using [C/M] and [N/M] measurements. However, we underline that these relations only apply to a certain range of labeled values since they used the range-bound eigenvalues, which prevents them from estimating the masses and ages of low metal abundance outlier stars in the LAMOST data.

Ness et al. (2016) also used the Cannon method, using masses measured directly from APOGEE spectra ($R \sim 22{,}500$) and ages estimated by isochrone fitting independent of carbon or nitrogen. Both the Martig et al. (2016b) relation and the Ness et al. (2016) catalog were calibrated on the same stellar sample (APOKASC). As highlighted in Martig et al. (2016b), the mass (and age) estimates for single stars must be used with great caution. For individual stars, the surface carbon and nitrogen abundances may not always reflect their current stellar masses,

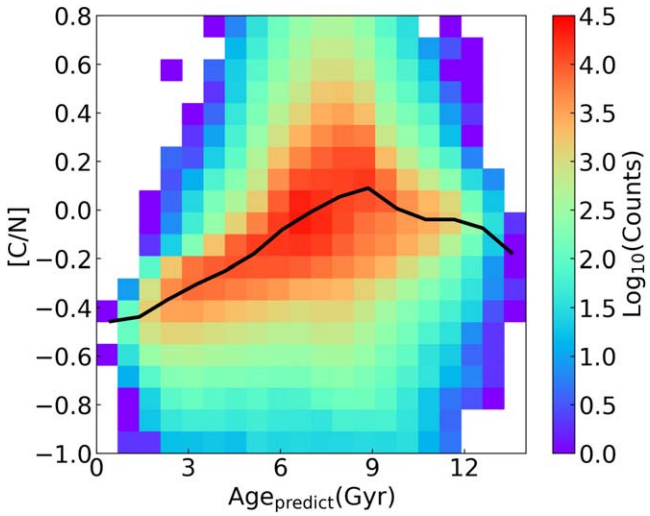

Figure 13. Relationship between the predicted age and the [C/N] ratio. The colors indicate the logarithmic values of the number of stars. The black line denotes the median value of the [C/N] ratio in each bin.

and it is possible that the presence of binary companions may have an impact. Therefore, their method may be better suited for statistical studies of large samples of stars and for

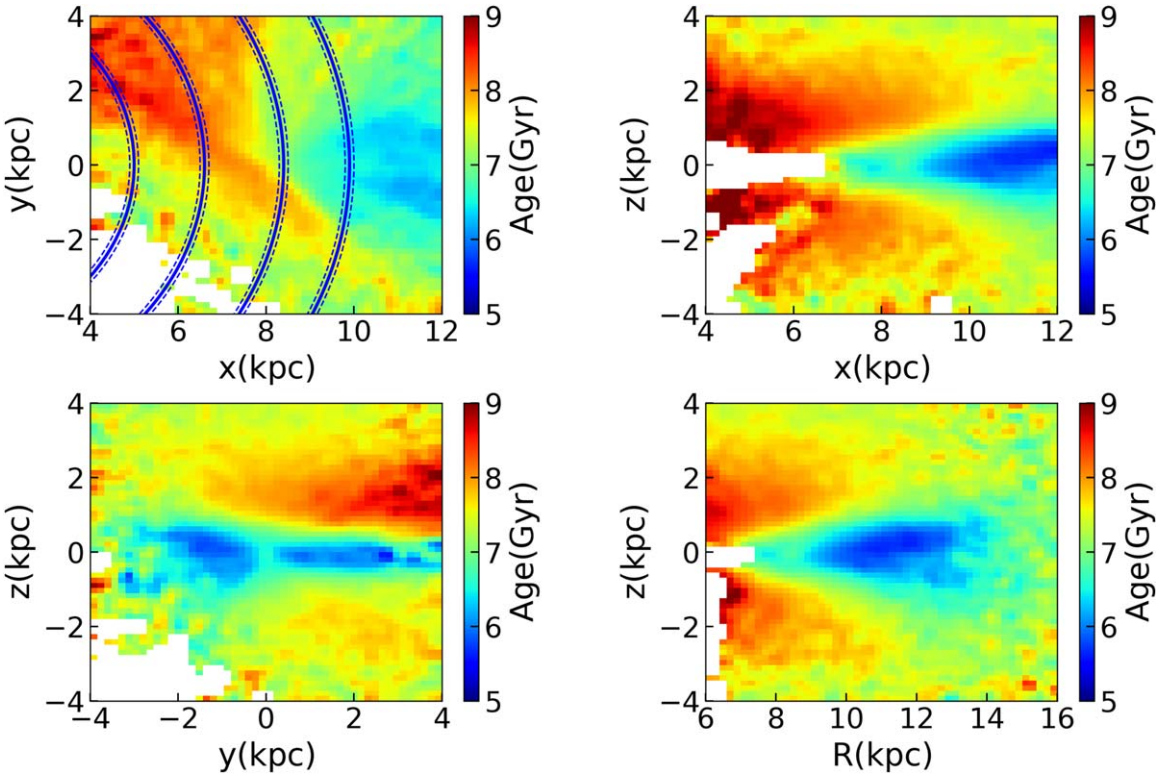

Figure 14. The spatial distribution of the 596,116 red giants for which we predict the age is color-coded. The lower-right panel uses Galactic cylindrical coordinates, while the first three panels represent Cartesian coordinates. The blue lines in the top-left panel indicate the four spiral arms from Reid et al. (2014).

comparing the properties of different populations. Recently, Leung et al. (2023) adopted a variational encoder-decoder method to create a publicly available stellar age catalog of 140,000 stars from APOGEE DR17, again using the age values of Miglio et al. (2021) as a training sample. When compared with the ages of astroNN, the overall systematics is about 25%. We find that the random errors from the comparison between ours and their ages amount to about 19%, but the systematics is not very relevant for ages below 9 Gyr.

Furthermore, Figure 11 (left panel) shows a comparison of the age estimates of our sample with the ages of the open clusters from Cantat-Gaudin et al. (2020). They used an artificial neural network trained with a mixture of simulated and real data (mainly from Bossini et al. 2019) to estimate the distance, age, and interstellar reddening of about 2000 clusters from Gaia DR2. The eight open clusters were selected by position, line-of-sight velocity, and [Fe/H] (referenced from Dias et al. 2021 and Donor et al. 2020). The horizontal error bars are derived from the uncertainty cited by Cantat-Gaudin et al. (2020), and the error bars in the *y*-direction are provided by the standard deviation of the cluster members we selected. In the left panel, we mainly use sky coordinates, proper motion, parallax, and isochrone fitting for the selection. We would like to note also that we have not enough metallicity and radial velocity information. Finally, the number of members of the above open clusters ranges from two to four stars.

One can readily see that our predicted ages matched well with the ages of the open clusters, with an overall bias of about 15% compared to the open cluster values. The systematics of NGC 6819 are slightly larger, around 1.63 Gyr; Berkeley 39 has the largest error bars. Except for Berkeley 39, NGC 6791, and Berkeley 17, the other open clusters have errors below 2 Gyr. We can also notice that the errors for older open clusters are overall larger than those for younger open clusters.

Spatial position, proper motion, radial velocity, and [Fe/H] are used as selection criteria for clusters' member stars. In case some stars do not have metallicity or radial velocity then we choose other criteria to select the memberships. In general, the selected member stars have a spatial position difference from the cluster of less than 1°, proper motion difference within 1.2 mas yr^{-1}, and [Fe/H] variation within 0.05 dex. The number of selected stars for each cluster are as follows: NGC 2420: 3, NGC 6819: 2, Berkeley 78: 2, NGC 2682: 3, NGC 1193: 4, Berkeley 39: 2, NGC 6791: 3, and Berkeley 17: 4.

In the right panel of Figure 11, we select the cluster member stars by crossmatching them directly with the equatorial coordinates of the cluster's star catalog, with a maximum error of no more than 1″. The final number of open cluster member stars ranges from two to nine. The overall bias compared to the age values of the open clusters is about 30%

Figure 12 shows the process of selecting cluster membership in our predicted sample using NGC 1193 as an example. First, we constrained the spatial position within a range of no more than 0.°7. Second, we further limited the proper motion to no more than 1 mas yr^{-1}. Third, we restricted the [Fe/H] values within a range of no more than 0.03 dex since member stars of a cluster are expected to originate from the same molecular cloud, and hence, share similar metallicity. Finally, comparing the selected member stars of the cluster to the PARSEC isochrone as a validation (Bressan et al. 2012).

4.3. Stellar Age–[C/N] Ratio Relation

It has been suggested long ago to use the [C/N] ratio from spectra as a proxy for RGB stellar ages: during the main

sequence, the CNO cycle in the star core determines the final relative abundances of carbon and nitrogen elements. The first dredge-up takes place as stars in the main-sequence phase evolve to the RGB branch stage, where the surface convective layer expands downward to the fusion material layer, and the material in the core is moved up to the surface by convective mixing. The depth of the convective envelope and the [C/N] ratio in the core are determined by the mass of the star. The mass and age of stars on giant branches are, therefore, closely related, which also implies that the [C/N] ratio can be used to infer stellar ages (Salaris et al. 2015; Das & Sanders 2019).

In Figure 13, we show the [C/N] ratio versus the predicted age. We calculate the median value in the star bins to show [C/N] as a function of the predicted age. For stars with ages less than 9 Gyr, the stellar age correlates well with the [C/N] ratio, as expected. For stellar ages larger than or equal to 9 Gyr, the ages seem to show an inverse correlation, but the number of stars in this age range is much smaller in our RGB sample, so this trend might be spurious. Using APOGEE full-spectrum data, Mackereth et al. (2019) applied a neural network-based model in an attempt to improve age estimation by examining the more complex relationship between age and surface abundance. This approach avoids the dependence of age estimates on the determination of individual abundance in a spectrum. They also point out that the age of sample stars may exceed the limit (10 Gyr) beyond which the spectral information no longer appears to be valid for age prediction.

4.4. Spatial Distribution of Stellar Ages

In Figure 14, we present the spatial distribution of the 596,116 RGB age distribution in Cartesian coordinates. The redder the regions, the older the median age of the stars. The three left panels clearly show that the age increases with the height of the plane. From the two right panels, it seems that the disk flaring can be detected. As expected, younger thin disks, older thick disks, and age transitions between halo components are naturally revealed here, and we look forward to using these stars to investigate the outer disk in greater detail.

5. Discussion

5.1. Age Determination of Other Random Parameter Combinations

As a method test, we randomly choose six parameters to predict age. As shown in Figure 15, displaying three examples of the training sample results in three different combinations of parameters. As can be seen from the distribution of age-relative errors and the mean and median age-relative errors in the figure, the mean relative errors are 17%–21%, and the median values are all below 15%. Therefore, it is feasible to use other combinations of stellar parameters for age prediction so that our model can achieve good accuracy. If we used a training data set with a larger sample size and better quality, the accuracy of our prediction results would be improved. Improving the prediction accuracy can also be done by starting with the asteroseismology parameters in the future since it has been shown that age predictions with asteroseismology parameters (e.g., $\nu_{\rm max}$ and $\Delta\nu$) have good accuracy.

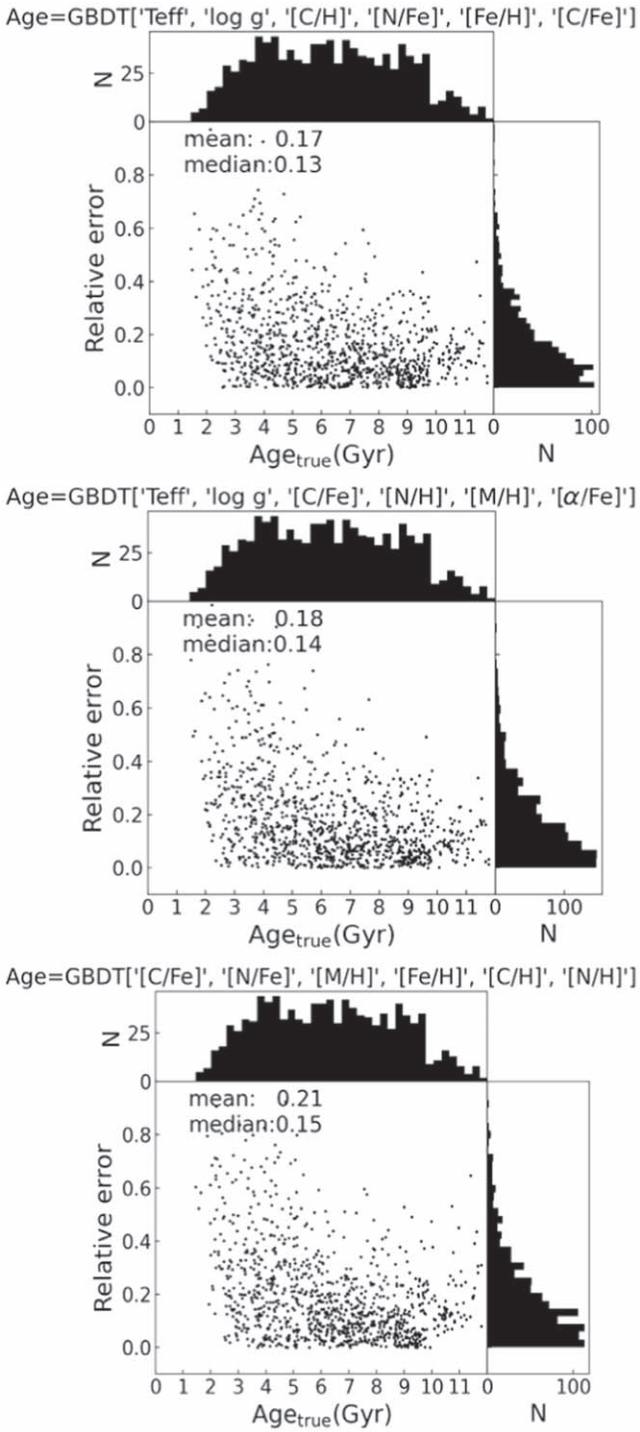

Figure 15. The stellar age predicted by other combinations of randomly chosen stellar parameters. The combinations of parameters from top to bottom are ($T_{\rm eff}$, log g, [C/H], [N/Fe], [Fe/H], [C/Fe]), ($T_{\rm eff}$, log g, [C/Fe], [N/H], [M/H], [α/Fe]), and ([C/Fe], [N/Fe], [M/H], [Fe/H], [C/H], [N/H]). The mean and median relative errors of the predicted ages are shown in the top-left corner of the three panels. It is clearly shown that the age can be determined by a variety of stellar parameters.

5.2. Possible Applications

These tests, along with the predictions shown in Figure 16, imply that many different parameters are correlated, as also mentioned in Ting & Weinberg (2022), who show that many elemental abundances can be predicted from other parameters, such as [Fe/H] and [Mg/Fe] (or [Fe/H] and age.

Ting & Weinberg (2022) also showed that cross-element correlations are more effective probes of a hidden structure than dispersion. In fact, some critical information on the elements cannot be simply inferred from the metallicity and α elements, and the residual correlation structure of the abundance trend might be important for stellar evolution studies, interstellar mixing, and the disk merger history.

The metallicity and chemical abundance are produced by the core-collapse supernovae (e.g., α/Fe), Type Ia supernovae ([Fe/H]), asymptotic giant branch (AGB) stars (Ce), neutron star mergers (Eu/Fe), etc.). One can find more details in Ting et al. (2012, 2017b) and Weinberg et al. (2019, 2022). Age is an extremely valuable tracer for the stellar evolution history and dynamical evolution of the MW disk. As a prospect, we suggest that one could use this sample to statistically investigate the disk structure, such as flaring and warp, using mono-age populations and disk heating history based on action angles (H.-F. Wang et al. 2024, in preparation; Frankel et al. 2020).

6. Conclusions

In this study, we carefully selected a sample of RGB stars in APOKASC-2 as a training sample and then trained the age prediction model using the GBDT machine-learning method aiming at estimating the ages of 596,116 RGB stars of LAMOST DR8. The correlation between stellar Eigen parameters and stellar ages is analyzed using the GBDT algorithm. We select the top six feature parameters in the correlation ranking with age to train the age prediction model, and the median absolute model error can reach 0.72 Gyr, and the median relative error can reach 11.6%.

After comparing the predicted ages with the results of other works, such as Gaia and APOGEE, we find that the overall trend is good, and the median relative error of the stellar age comparison is around 16%. When comparing with the open clusters, our predicted ages are in good agreement with their ages, with the final uncertainty being about 15%–30%.

As a validation of the method, the linear relationship between the reliably predicted age and [C/N] and the expected vertical age gradient of the Galactic disk are also reproduced. Moreover, we find that our method is not only suitable for age determination but can also be applicable to other atmospheric parameters.

We also discuss the effects of different combinations of input feature parameters for age prediction. The mean relative errors range from 17%–21%, and the median relative errors are all below 15%. It is worth further exploring the stellar parameters, including basic stellar parameters, abundance parameters, age, and even distance and extinction, in the future.

Acknowledgments

We would like to thank the anonymous referee for the very helpful and insightful comments. H.F.W. is supported by the Department of Physics and Astronomy of Padova University through the 2022 ARPE grant: Rediscovering our Galaxy with Machines. The Guo Shou Jing Telescope (LAMOST) is a National Major Scientific Project built by the Chinese Academy of Sciences. Funding for the project has been provided by the National Development and Reform Commission. LAMOST is operated and managed by the National Astronomical Observatories, Chinese Academy of Sciences. This work has also made use of data from the European Space Agency (ESA) mission Gaia (https://www.cosmos.esa.int/gaia), processed by the Gaia Data Processing and Analysis Consortium (DPAC; https://www.cosmos.esa.int/web/gaia/dpac/consortium). Funding for the DPAC has been provided by national institutions, in particular, the institutions participating in the Gaia Multilateral Agreement.

Appendix
Other Predicted Stellar Chemical Parameters

To illustrate the correlation between different feature parameters, we use the method and six stellar parameters described above to predict the three remaining feature parameters and compare the predicted values with the original parameters (see Figure 16). In all panels of Figure 16, the scatter points representing the stellar parameter values are almost uniformly distributed on both sides of the red line, indicating that our model is able to predict the stellar feature parameters robustly. The well-predicted results also show again that there is indeed a good consistency between these stellar feature parameters. The dispersion in Figure 16 (values in left corner) also evidence that these predicted parameters are reasonable considering the uncertainties of the stellar parameters for any survey data sets.

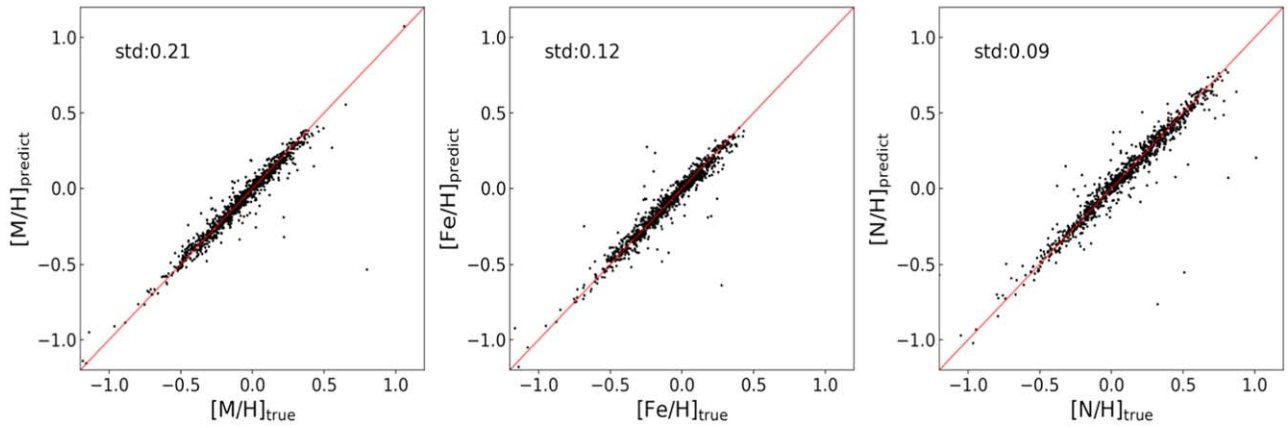

Figure 16. Predictions for the remaining three stellar features ([M/H], [Fe/H], and [N/H]) on the basis of the six stellar features of the predicted age. The dispersion is shown in the left-top corner of each panel.

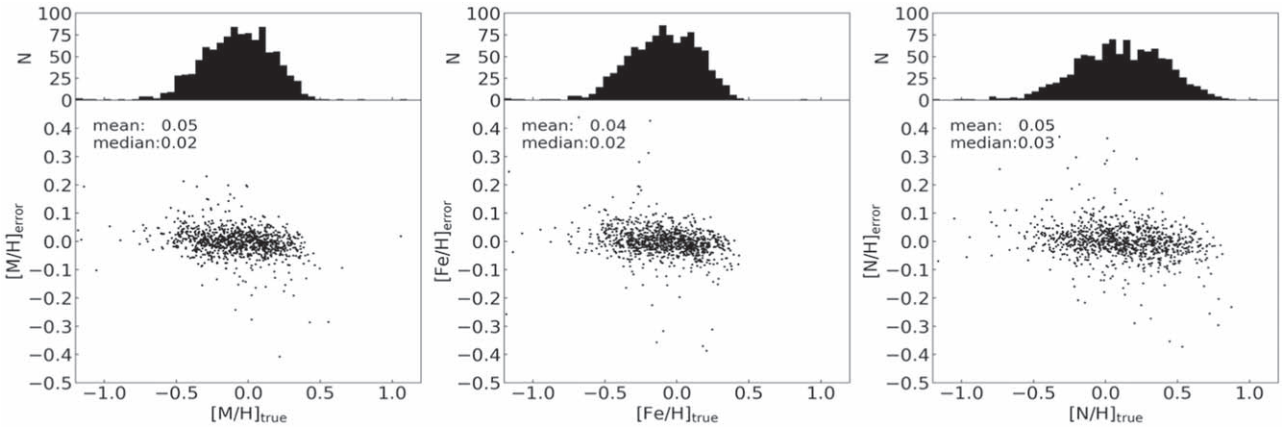

Figure 17. The error distribution of the predicted features is arranged in the same order as in Figure 16. The histogram indicates the distribution of the number of stars over the values of the characteristic parameters. The predicted feature parameters obtained are in agreement with the true features for the overall trend with small relative errors.

In Figure 17, we show the error distributions for the three characteristic parameters as a complement to Figure 16, implying that our model has a certain degree of reliability in predicting these correlated feature parameters. Although there is some dispersion, we expect that the method may exhibit improved performance in parameter prediction when the training sample becomes sufficiently large and precise enough in the future. In the meantime, we believe the precision of these parameters might be improved by finding the feature parameters that are better correlated with them in the model training so that our method would surely work not only with suitable atmospheric parameters but also with stellar age.

ORCID iDs

Hai-Feng Wang https://orcid.org/0000-0001-8459-1036
Giovanni Carraro https://orcid.org/0000-0002-0155-9434
Lorenzo Spina https://orcid.org/0000-0002-9760-6249

References

Anders, F., Chiappini, C., Rodrigues, T. S., et al. 2017, A&A, 597, A30
Anders, F., Gispert, P., Ratcliffe, B., et al. 2023, A&A, 678, A158
Andrae, R., Fouesneau, M., Sordo, R., et al. 2023, A&A, 674, A27
Bossini, D., Vallenari, A., Bragaglia, A., et al. 2019, A&A, 623, A108
Bouret, J.-C., Donati, J.-F., Martins, F., et al. 2008, MNRAS, 389, 75
Bovy, J., Rix, H.-W., Schlafly, E. F., et al. 2016, ApJ, 823, 30
Bressan, A., Marigo, P., Girardi, L., et al. 2012, MNRAS, 427, 127
Brott, I., & Hauschildt, P. H. 2005, Proc.Gaia Symposium "The Three-Dimensional Universe with Gaia", ed. C. Turon, K. S. O'Flaherty, & M. A. C. Perryman, 565
Buder, S., Sharma, S., Kos, J., et al. 2021, MNRAS, 506, 150
Cantat-Gaudin, T., Anders, F., Castro-Ginard, A., et al. 2020, A&A, 640, A1
Casali, G., Magrini, L., Tognelli, E., et al. 2019, A&A, 629, A62
Casamiquela, L., Soubiran, C., Jofré, P., et al. 2021, A&A, 652, A25
Chaplin, W. J., & Miglio, A. 2013, ARA&A, 51, 353
Chen, D.-C., Xie, J.-W., Zhou, J.-L., et al. 2021, ApJ, 909, 115
Chen, T., & Guestrin, C. 2016, KDD '16: Proc 22nd ACM SIGKDD Int. Conference on Knowledge Discovery and Data Mining (New York: ACM)
Choi, J., Dotter, A., Conroy, C., et al. 2016, ApJ, 823, 102
Ciucă, I., Kawata, D., Miglio, A., et al. 2021, MNRAS, 503, 2814
Ciucă, I., Kawata, D., Ting, Y.-S., et al. 2024, MNRAS, 528, L122
Conroy, C., Weinberg, D. H., Naidu, R. P., et al. 2022, arXiv:2204.02989
Cui, X.-Q., Zhao, Y.-H., Chu, Y.-Q., et al. 2012, RAA, 12, 1197
Das, P., & Sanders, J. L. 2019, MNRAS, 484, 294
Delgado Mena, E., Moya, A., Adibekyan, V., et al. 2019, A&A, 624, A78
De Silva, G. M., Freeman, K. C., Bland-Hawthorn, J., et al. 2015, MNRAS, 449, 2604
Dias, W. S., Monteiro, H., Moitinho, A., et al. 2021, MNRAS, 504, 356
Donor, J., Frinchaboy, P. M., Cunha, K., et al. 2020, AJ, 159, 199
Feltzing, S., Howes, L. M., McMillan, P. J., et al. 2017, MNRAS, 465, L109
Fitzpatrick, E. L. 1999, PASP, 111, 63
Frankel, N., Sanders, J., Ting, Y.-S., & Rix, H.-W. 2020, ApJ, 896, 15
Gallart, C., Bernard, E. J., Brook, C. B., et al. 2019, NatAs, 3, 932
Gustafsson, B., Edvardsson, B., Eriksson, K., et al. 2008, A&A, 486, 951
Hayden, M. R., Sharma, S., Bland-Hawthorn, J., et al. 2022, MNRAS, 517, 5325
He, X.-J., Luo, A.-L., & Chen, Y.-Q. 2022, MNRAS, 512, 1710
Ho, A. Y. Q., Ness, M. K., Hogg, D. W., et al. 2017b, ApJ, 836, 5
Ho, A. Y. Q., Rix, H.-W., Ness, M. K., et al. 2017a, ApJ, 841, 40
Huang, Y., Schönrich, R., Zhang, H., et al. 2020, ApJS, 249, 29
Jofré, P., Jackson, H., & Tucci Maia, M. 2020, A&A, 633, L9
Kordopatis, G., Schultheis, M., McMillan, P. J., et al. 2023, A&A, 669, A104
Lagarde, N., Robin, A. C., Reylé, C., et al. 2017, A&A, 601, A27
Lebreton, Y., & Reese, D. R. 2020, A&A, 642, A88
Leung, H. W., & Bovy, J. 2019, MNRAS, 483, 3255
Leung, H. W., Bovy, J., Mackereth, J. T., et al. 2023, MNRAS, 522, 4577
Li, Q.-D., Wang, H.-F., Luo, Y.-P., et al. 2022, ApJS, 262, 20
Li, X., Yang, P., Wang, H.-F., et al. 2023, OJAp, submitted (arXiv:2310.01311)
Liu, C., Deng, L.-C., Carlin, J. L., et al. 2014, ApJ, 790, 110
López-Corredoira, M., Allende Prieto, C., Garzón, F., et al. 2018, A&A, 612, L8
Lu, Y. X., Ness, M. K., Buck, T., et al. 2022, MNRAS, 512, 4697
Mackereth, J. T., Bovy, J., Leung, H. W., et al. 2019, MNRAS, 489, 176
Mackereth, J. T., Miglio, A., Elsworth, Y., et al. 2021, MNRAS, 502, 1947
Majewski, S. R., Schiavon, R. P., Frinchaboy, P. M., et al. 2017, AJ, 154, 94
Martig, M., Fouesneau, M., Rix, H.-W., et al. 2016b, MNRAS, 456, 3655
Martig, M., Minchev, I., Ness, M., et al. 2016a, ApJ, 831, 139
Masseron, T., & Gilmore, G. 2015, MNRAS, 453, 1855
McMillan, P. J., Kordopatis, G., Kunder, A., et al. 2018, MNRAS, 477, 5279
Miglio, A., Chiappini, C., Mackereth, T., et al. 2021, yCat, J/A + A/645/A85
Miglio, A., Chiappini, C., Mosser, B., et al. 2017, AN, 338, 644
Miglio, A., Montalbán, J., & Noels, A. 2012, in Red Giant Branchs as Probes of the Structure and Evolution of the Milky Way, ed. A. Miglio, J. Montalban, & A. Noels (Berlin: Springer), 26
Mints, A., & Hekker, S. 2017, A&A, 604, A108
Montalbán, J., Mackereth, J. T., Miglio, A., et al. 2021, NatAs, 5, 640
Ness, M., Hogg, D. W., Rix, H.-W., et al. 2015, ApJ, 808, 16
Ness, M., Hogg, D. W., Rix, H.-W., et al. 2016, ApJ, 823, 114
Ness, M. K., Johnston, K. V., Blancato, K., et al. 2019, ApJ, 883, 177
Nissen, P. E. 2015, A&A, 579, A52
Nissen, P. E. 2016, A&A, 593, A65
Nissen, P. E., Silva Aguirre, V., Christensen-Dalsgaard, J., et al. 2017, A&A, 608, A112
Noels, A., & Bragaglia, A. 2015, in Asteroseismology of Stellar Populations in the Milky Way, ed. A. Miglio (Cham: Springer), 167
Pedregosa, F., Varoquaux, G., Gramfort, A., et al. 2011, J. Mach. Learn. Res., 12, 2825
Pinsonneault, M. H., Elsworth, Y., Epstein, C., et al. 2014, ApJS, 215, 19
Pinsonneault, M. H., Elsworth, Y. P., Tayar, J., et al. 2018, ApJS, 239, 32
Rauer, H., Catala, C., Aerts, C., et al. 2014, ExA, 38, 249

Reid, M. J., Menten, K. M., Brunthaler, A., et al. 2014, ApJ, 783, 130
Rendle, B. M., Miglio, A., Chiappini, C., et al. 2019, MNRAS, 490, 4465
Rix, H.-W., & Bovy, J. 2013, A&ARv, 21, 61
Salaris, M., Pietrinferni, A., Piersimoni, A. M., et al. 2015, A&A, 583, A87
Sanders, J. L., & Das, P. 2018, MNRAS, 481, 4093
Santiago, B. X., Brauer, D. E., Anders, F., et al. 2016, A&A, 585, A42
Schonhut-Stasik, J., Zinn, J. C., Stassun, K. G., et al. 2024, AJ, 167, 50
Scilla, D. 2016, JPhCS, 703, 012002
Sharma, S., Stello, D., Buder, S., et al. 2018, MNRAS, 473, 2004
Shulyak, D., Reiners, A., Engeln, A., et al. 2017, NatAs, 1, 0184
Silva Aguirre, V., Bojsen-Hansen, M., Slumstrup, D., et al. 2018, MNRAS, 475, 5487
Silva Aguirre, V., Stello, D., Stokholm, A., et al. 2020, ApJL, 889, L34
Soderblom, D. R. 2010, ARA&A, 48, 581
Spina, L., Meléndez, J., Karakas, A. I., et al. 2016, A&A, 593, A125
Spina, L., Meléndez, J., Karakas, A. I., et al. 2018, MNRAS, 474, 2580
Stello, D., Huber, D., Sharma, S., et al. 2015, ApJL, 809, L3
Ting, Y.-S., Conroy, C., Rix, H.-W., et al. 2019, ApJ, 879, 69
Ting, Y.-S., Freeman, K. C., Kobayashi, C., De Silva, G. M., & Bland-Hawthorn, J. 2012, MNRAS, 421, 1231
Ting, Y.-S., Hawkins, K., & Rix, H.-W. 2018, ApJL, 858, L7
Ting, Y.-S., & Rix, H.-W. 2019, ApJ, 878, 21
Ting, Y.-S., Rix, H.-W., Conroy, C., Ho, A. Y. Q., & Lin, J. 2017b, ApJL, 849, L9
Ting, Y.-S., & Weinberg, D. H. 2022, ApJ, 927, 209
Tucci Maia, M., Ramírez, I., Meléndez, J., et al. 2016, A&A, 590, A32
Valentini, M., Chiappini, C., Miglio, A., et al. 2016, AN, 337, 970
Viscasillas Vázquez, C., Magrini, L., Casali, G., et al. 2022, A&A, 660, A135
Wang, C., Huang, Y., Yuan, H., et al. 2022b, ApJS, 259, 51
Wang, C., Huang, Y., Zhou, Y., et al. 2023c, A&A, 675, A26
Wang, H.-F., Carlin, J. L., Huang, Y., et al. 2019, ApJ, 884, 135
Wang, H.-F., Chrobáková, Ž., López-Corredoira, M., & Sylos Labini, F. 2023a, ApJ, 942, 12
Wang, H.-F., Hammer, F., Yang, Y. B., et al. 2022a, ApJL, 940, L3
Wang, H.-F., Huang, Y., Zhang, H.-W., et al. 2020c, ApJ, 902, 70
Wang, H.-F., Liu, C., Xu, Y., et al. 2018b, MNRAS, 478, 3367
Wang, H.-F., López-Corredoira, M., Carlin, J. L., et al. 2018a, MNRAS, 477, 2858
Wang, H.-F., López-Corredoira, M., Huang, Y., et al. 2020a, MNRAS, 491, 2104
Wang, H.-F., López-Corredoira, M., Huang, Y., et al. 2020b, ApJ, 897, 119
Wang, H.-F., Yang, Y.-B., Hammer, F., et al. 2023b, A&A, submitted (arXiv:2204.08542)
Weinberg, D. H., Holtzman, J. A., Hasselquist, S., et al. 2019, ApJ, 874, 102
Weinberg, D. H., Holtzman, J. A., Johnson, J. A., et al. 2022, ApJS, 260, 32
Wilson, J. C., Hearty, F. R., Skrutskie, M. F., et al. 2019, PASP, 131, 055001
Wu, Y., Xiang, M., Bi, S., et al. 2018, MNRAS, 475, 3633
Wu, Y., Xiang, M., Zhao, G., et al. 2023, MNRAS, 520, 1913
Xiang, M., & Rix, H.-W. 2022, Natur, 603, 599
Xiang, M., Ting, Y.-S., Rix, H.-W., et al. 2019, ApJS, 245, 34
Zhang, X., Green, G. M., & Rix, H.-W. 2023, MNRAS, 524, 1855
Zinn, J. C., Stello, D., Elsworth, Y., et al. 2022, ApJ, 926, 191